Prediction of accumulated cyclone energy in tropical cyclone over the western North Pacific in autumn

Yanjie Wu[1,2] · Fei Huang[1,2,3] · Shibin Xu[1,2] · Wen Xing[4]

Abstract

Tropical cyclones (TCs) are affected significantly by the climate system and can provide feedbacks. TC activities are important for weather forecasting and climate predictions. Here, we focused on the spatial distribution of accumulated cyclone energy (ACE) and its seasonal prediction. To predict the ACE distribution over the western North Pacific (WNP) in autumn, we established a physical-empirical model. Analyzing 36 years observations (1979–2014) of ACE over the WNP reveals two physically predictable modes. The sea surface temperature (SST) in the southwest Pacific and central Pacific affect the first mode through the low-level circulations. At the same time, the SST in the Gulf of Alaska and the sea-ice concentration in the Beaufort Sea affect the first mode through the circumglobal teleconnection. The development of the eastern Pacific El-Niño and anomalous SST over the North Pacific affect the second mode through the vertical wind shear and low-level circulation. The sea-ice concentration in the Greenland Sea induce an upper-level circulation anomaly over the WNP and affect the second mode. Physically meaningful predictors were selected according to the controlling mechanisms of the two modes. The cross-validated hindcast results demonstrated that the principal components of the two modes are predicted with correlation coefficients of 0.68 and 0.63. Thus, the two modes are predictable. The pattern correlation coefficient skill of the ACE spatial pattern is 0.26, which is significant at the 99% confidence level. The temporal correlation coefficient skill reaches 0.21 over major regions influenced by TCs. To validate the real-time predictability of the model, independent tests were performed on the last three years (2015, 2016 and 2017), and the results show that the pattern correlation coefficients between the observations and the predictions are 0.39, 0.70, and 0.41, respectively.

Keywords Accumulated cyclone energy · Western north pacific · Predictable mode analysis · Sea surface temperature · Arctic sea ice

✉ Shibin Xu
  xushibin@ouc.edu.cn

[1] Physical Oceanography Laboratory, Ocean University of China, Qingdao 266100, China

[2] Laboratory for Ocean and Climate Dynamics, Pilot National Laboratory for Marine Science and Technology (Qingdao), Qingdao 266100, China

[3] Ningbo Collaborative Innovation Center of Nonlinear Hazard System of Ocean and Atmosphere, Ningbo University, Ningbo 315000, China

[4] Department of Atmospheric and Oceanic Sciences, University of Colorado, Boulder, CO 80309, USA

1 Introduction

Tropical cyclones (TCs) are intense atmospheric vortices that develop over warm tropical or subtropical oceans. TC activity includes TC genesis, development and tracks, which results from multiscale interactions. TC tracks are mostly affected by large-scale atmospheric general circulation (Wu and Emanuel 1993; Wu and Kurihara 1996; Wang and Holland 1996), beta drift (Chan and Gray 1982; Holland 1983, 1984; Carr and Elsberry 1990) and their interactions (Demaria 1985; Evans et al. 1991; Wang et al. 1998). The climate systems that influence TC activity over the western North Pacific (WNP) include the El Niño-Southern Oscillation (ENSO) (Chan 1985; Camargo et al. 2007; Wang and Chan 2002; Hu et al. 2018), subtropical high (Luo 2001), Indian Ocean sea surface temperature (SST) (Zhan et al. 2011; Du et al. 2011), Madden–Julian oscillation (Maloney and

Hartmann 2001; Camargo et al. 2009; Lee et al. 2018) sea ice (Fan 2007; Deng et al. 2018), Hadley cell (Lander 1994; Camargo et al. 2007) quasi-biennial oscillation (Chan 1995), summer monsoons (Lander 1994; Camargo et al. 2007), Arctic oscillation (Choi and Byun 2010), the mid-Pacific trough (Wu et al. 2015; Wang and Wu 2016; Deng et al. 2018; Hu et al. 2018), the westerlies (Dong and Neumann 1986) and so on.

As an important component of the global climate system, TC activities may provide cross-scale feedbacks to the climate system. Bell et al. (2000) proposed that the accumulated cyclone energy (ACE), which is defined as the accumulated wind power of TCs, is able to quantify TC activity. The latest research has shown that TC ACE in a particular region over the WNP can modulate the amplitude of ENSO (Wang et al. 2019) and affect the interannual variability of the climate system. Thus, the prediction of TC ACE is important to climate prediction, but it is a difficult problem that needs to be solved. Some studies have focused on the prediction of ACE over different basins. Lea and Saunders (2003) predicted the North Atlantic yearly ACE index with 925-hPa zonal wind and SST over the main development region. Since 2000, the Tropical Storm Risk program has issued basin-wide ACE prediction and provided probabilistic outlook forecasts from March to August over the North Atlantic every year using SST (Lloyd-Hughes et al. 2004). Klotzbach (2014) used 2-m air temperature and 200-hPa zonal wind to predict the North Atlantic ACE index from June to October. Based on the circulation and SSTs predicted by the second version of the Climate Forecast System, Zhan and Wang (2016) used the SST gradient, vertical wind shear (VWS), Niño 3.4 SST and the southwestern Pacific SST to predict ACE over the WNP. However, the previous seasonal forecast of ACE addresses the total ACE over a whole oceanic basin, which not focus on the spatial distribution of ACE. This study focuses on both the spatial and temporal prediction of ACE over the WNP, including the South China Sea (SCS).

In previous studies, most predictions of ACE used SST as a predictor. Fan (2007) proposed that Arctic sea ice affects the TC frequency over the WNP. The loss of Arctic sea ice induces the western part of the WNP to favor TC genesis and development, which results westward shift in TC activity (Deng et al. 2018). Moreover, the emergence of surface-based Arctic amplification caused by fast melting of Arctic sea ice affects global climate change by planetary wave amplification (Screen and Simmonds 2013; Cohen et al. 2014), which may result in many disastrous weather events (Tang et al. 2014), such as freezing rain (Niu et al. 2015), extremely high temperatures (Zhou and Huang 2015), and extreme low temperatures (Hu et al. 2015), which frequently appear in mid-latitudes. In other words, the Arctic sea ice as a type of external forcing may be a good long-lead predictor for mid-latitude weather and extreme events predictions in

the coming decades (Cohen et al. 2014). Whether the Arctic sea ice will contribute to ACE predictions is still unknown, and we need to further investigate this issue further. In this study, we attempt to predict the spatial pattern of ACE in autumn (September–November) using the predictable mode analysis (PMA) method (Wang et al. 2007) to build the physical-empirical (P–E) model, which is introduced in detail in the methods. We focus on autumn because the mean TC intensity, which is based on the ratio of super typhoon frequency and storms, is strongest this season (Xu and Huang 2010). The ratio of the number of TCs with rapid intensification to the total number of TCs (Wang and Zhou 2008) is also the highest among in this season. However, TC ACE in autumn is not well investigated compared to the typical TC season (July–October) over the WNP.

This paper is organized as follows. The data and methods are described in Sect. 2. Section 3 briefly introduces the climatology of ACE in autumn over the WNP. Section 4 shows the two dominant modes of ACE, the dipole mode and the triple mode, and investigates the possible mechanism by which the tropical ocean and the Arctic affect the ACE of these two modes. The P–E model is built in Sect. 5, and the predictability, including the predictability from 1979 to 2014 and the real-time predictions from 2015 to 2017, is also discussed in this section. Section 6 presents conclusions and discussion.

2 Data and methods

2.1 Data

The TC data used in this paper were the best track data (BTD) provided by the Japan Meteorological Agency (JMA) for the period from 1979 to 2017. ACE, which calculates the sum of the maximum sustained wind speed squared for each 6-h interval, is defined here (Bell et al. 2000; Kim et al. 2013).

$$\text{ACE} = \sum_{i=1}^{N} \sum_{t_{oi}}^{t_{fi}} v(t)^2, \tag{1}$$

where t represents the lifetime of each TC, N is the total number of TCs, t_{oi} is the original record of each TC, t_{fi} is the final record of each TC and $v(t)$ is the maximum sustained wind speed for each 6 h interval according to the BTD. Only the lifetime maximum intensity of a TC above a tropical storm ($v_{max} \geq 17.2$) m/s can be considered in this study. Similarly, the lifetime with $v(t) < 17.2$ m/s is regarded as an immature disturbance or a collapsed tropical cyclone, which is excluded in our study. Since we focused on the TC intensity prediction in autumn, which is different from the traditional TC season (JJASO, from June to October),

we defined the seasonal ACE from September to November (SON) over both the SCS and the WNP. ACE analysis was performed on the original data based on grids of $5° \times 5°$ in this study. Except for JMA, numerous agencies published BTD over the WNP, such as the Joint Typhoon Warning Center (JTWC), China Meteorological Agency (CMA), and the Hong Kong Observatory also contribute their observation of tropical cyclone to public. To avoid the single dataset bias on this study, as a comparison, we also used BTD from CMA (Ying et al. 2014) from 1979 to 2014 and BTD from JTWC with the same time range in the statistical section. Previous studies compared the differences between BTDs form numerous agencies. Though the differences in TC tracks among these data sets are negligibly small, the TCs in the BTD from JTWC tends to more intensity (Song et al. 2010; Barcikowska et al. 2012). Knapp and Kruk (2010) showed the difference in the mean deviation of the maximum sustain windspeed among BTD is largely linear and JMA slightly differs from CMA after the homogenous procedures. Thus the TC ACE based on the BTD provided by JTWC is larger than others, while their spatial distributions and interannual variations are similar. All TCs from different datasets were calculated in this paper and were chosen by the same criterion; their units were first changed from knots to meters per second.

The monthly mean atmospheric circulation data were obtained from the National Center for Environment Prediction (NCEP) Reanalysis1 dataset. The monthly SST data were from the Hadley Centre Sea Surface Temperature dataset 1 (HadISST1). This study used sea ice concentration (SIC) data from the National Snow and Ice Data Center (NSIDC) for the period 1979–2017. All climatology and anomalous calculations in this paper were based on the period from 1979 to 2014.

2.2 Methods: predictable mode analysis

Wang et al. (2007) first proposed the PMA method to evaluate the potential predictability and build a predictive model of the element field. This method has been used for estimating the predictability of anomalous anticyclones over the WNP (Wang et al. 2013), Asian summer rainfall (Yim et al. 2014), and other features (e.g., Yim et al. 2015; Xing et al. 2016, 2017).

The PMA method has three steps. First, the predictable mode observes frequent patterns of variability divided by empirical orthogonal function (EOF) analysis, which requires the variance contribution to occupy a large proportion of the total variance. Second, the prediction of each empirical pattern provides the dynamic basis with physical interpretation. In addition, a P–E prediction model is established by the principal component (PC) of each mode. Third, the P–E model uses retrospective predictions to confirm the

potential predictability of the predictable mode. We applied the cross-validation method to make a retrospective forecast for testing the hindcast experiment skills (Michaelsen 1987). For the retrospective forecast, we separated training and prediction samples and took every 3 years as targets to be predicted at each step. The PCs of target years were predicted using the multilinear regression equation to predict the root in the corresponding training period.

In this study, we selected physically consequential predictors from the anomalous fields of SST and SIC, which reflect influences on the mid-latitude atmospheric circulation. Compared to oceanic changes, the atmospheric process is relatively fast, and capturing signals of this process to make long-term forecasts is difficult. Changes in SST and Arctic SIC were applied to oceanic heat conditions, which include signals of heat transport and affected atmospheric circulations. These predictors were searched by identifying persistent signals from the previous spring to summer, with an average of three months per season. Following the process of finding predictors, we speculated about the physical mechanisms that could explain the relationship between ACE and these predictors. We used regression analyses to find these possible predictors and focused on those significant at the 95% confidence level according to Student's t-test. After choosing predictors, stepwise multilinear regression was used to build the P–E model, and each chosen predictor significantly increased the regressed variation via the standard F test (Panofsky and Brier 1968).

Since the P–E model considers only the value of ACE in the real-time prediction, determining whether TCs occurred in each grid was not possible. Therefore, the ACE at marginal regions was always calculated with a value but was actually zero. We used the regression estimation of event probability (REEP; Miller 1964) to discuss the occurrence of TCs in each grid. REEP first assigns a value of one or zero to represent that one process is or is not happening, and then uses multilinear regression to build an equation based on the predictors (also one or zero). Finally, the medians (the mean of the minimum probability when a process happens and the maximum probability when a process disappears) are used to distinguish whether TCs appeared. When the event probability was larger than the median, we considered the calculated value to be true. Conversely, the calculated value was replaced by zero when the event probability was less than the median.

3 Climatology of ACE over the WNP in autumn

The time series of ACE over the WNP in autumn (Fig. 1a) shows a significant interannual variation but has no consistent interdecadal trend. The 36-year mean ACE is
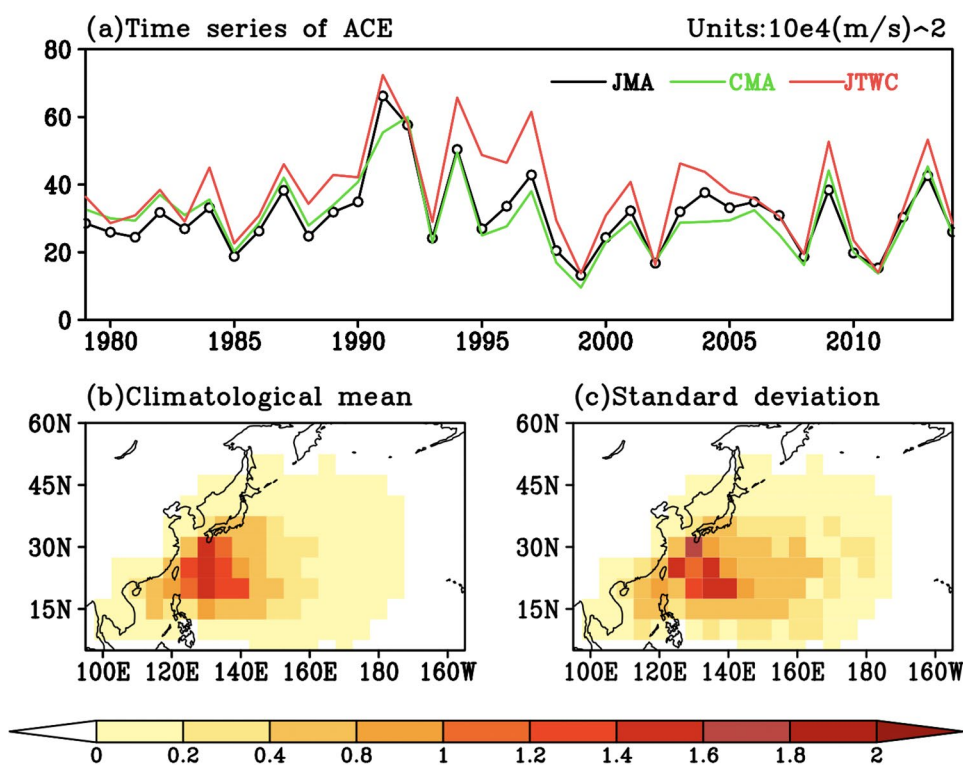
309,442 m^2/s^2, and the standard deviation is 111,975 m^2/s^2. The maximum ACE over the WNP is 661,909 m^2/s^2, while the minimum value of ACE is 131,949 m^2/s^2. These time series based on JTWC and JMA BTD have characteristics similar to the maximum value in 1991, except that the maximum value in the CMA data occurs in 1992. The correlation coefficient of the ACE time-series between JMA and CMA is 0.93 while the correlation coefficient between JMA and JTWC is 0.91, and the correlation coefficient of ACE between CMA and JTWC is 0.87. These values mean that the time series of ACE over the WNP differ slightly among different datasets. This result occurs because the differences between JTWC and CMA/JMA are largely linear, while the differences between JMA and CMA are much smaller (Knapp and Kruk 2010).

Figure 1b shows the spatial distribution of the long-term mean ACE in the WNP, which is largely coherent with the pattern of the ACE standard deviation shown in Fig. 1c. These results are based on the BTD from JMA for 1979–2014. The region (120° E–140° E; 15° N–30° N) represents the highest standard deviation, which is south of the Japan islands and near the East Asia mainland. High values of ACE over these regions indicate that the coastal regions of China, Japan, South Korea, and the Philippines experience large hazardous events (such as high wind and heavy precipitation). Therefore, the prediction of the ACE

distribution over the WNP is meaningful for East Asia. The pattern correlation coefficient of the ACE long-term mean pattern reaches 0.99 between JMA and CMA/JTWC, which implies less difference in their spatial distributions.

Based on the statistical climatology of ACE (Fig. 1b), we consider the area of (5°–60° N, 95° E–165° W) as the target region in the following sections, covering 12×23 grids over the WNP and SCS. A total of 126 grids contained TC activity from 1979 to 2014 derived from JMA. Additionally, 142 and 130 grids contained TC activity based on BTD from CMA and JTWC, respectively.

4 Leading EOF modes of ACE

Due to the lack of satellite data before the 1970s, we used ACE anomalies from 1979 to 2014 to perform EOF analysis to avoid possible inaccurate TC observations. Based on North's rule (North et al. 1982), the two leading EOF modes are significantly separated from each other and the remainder of the EOF modes. The two leading EOF modes of ACE account for 19.54% and 15.19% of the total variance. In comparison, they account for 22.84% and 12.12% of the total variance based on the BTD from CMA and 22.92% and 13.40% of the total variance based on the BTD from JTWC. The pattern correlation coefficients of the first leading EOF

mode from the three datasets are 0.94 and 0.94, while the pattern correlation coefficients are 0.64 and 0.66 for the second leading EOF mode between JMA and JTWC/CMA. In this section, we discuss the characteristics of ACE patterns and the regression/correlation maps of the atmospheric circulations associated with the first two modes. The PCs used in the regression/correlation analysis in the following section are based on JMA BTD because of small difference among the three datasets, and because the JMA is the official monitor for TC over the WNP.

4.1 The first mode: dipole mode

The spatial pattern of the first mode (EOF1) is characterized by a dipole distribution in 110°–155° E, 10°–40° N. This mode represents the TC dipole activity shown in Fig. 2a. The high positive center is located in the Philippine Sea, and the whole positive area reaches the line of 170° E. In contrast, the negative center shows a slope shaping, which from the East China Sea through Taiwan Island, and then ends at the SCS. Thus, we define the first mode as the dipole ACE mode. The principal component of this mode (PC1) shows an interannual variability of dipole ACE with peak values in 1991 and 2009 (Fig. 2b). In this mode, negative anomalies appear over the SCS and the Philippine Sea, and large positive anomalies are present over the region of 130° E–145° E, 10°–40° N, that is, over the WNP south of the Japan islands. This result means that more TCs affect the Philippine Sea and Japan islands but fewer TCs affect South China and the Philippine islands when PC1 is positive.

To determine the atmospheric circulation effect on the dipole mode, the regression maps of geopotential height in the upper troposphere (200 hPa) and mid-troposphere (500 hPa) for June–August (JJA) and SON, with PC1 referring to JMA ACE, are depicted in Fig. 3. The significant positive geopotential height anomalies at 200 hPa are located over western Europe, Siberia, and northern Canada, while negative geopotential height anomalies are located from west to east over the Ural Mountains, eastern Siberia, and the region from the North Atlantic to Greenland (Fig. 3a). They make up an anomalous wave train, similar to the circumglobal teleconnection proposed by Ding and Wang (2005) and Ding et al. (2011), and the shape of the wave train is straight in summer. These anomalous waves change to a sloping shape from 60° N to 40° N in autumn (Fig. 3b). Their positive centers move to the Ural Mountains, northeast of the Japan islands, and Hudson Bay at 200 hPa. The vertical feature of the anomalous wave train is vital to show how the large-scale atmosphere affects the dipole mode. Figure 3c shows the section along the straight line at 60° N in summer, and the anomalous waves train shows barotropic features. The result remains consistent in autumn, in which the section of the sloping line in Fig. 3d is also a barotropic feature that crosses the abnormal centers in Fig. 3b. The barotropic feature in autumn leads to a higher geopotential height center over northern Japan, north of the WNP subtropical high (WPSH), causing variations in the WPSH and wind at 500 hPa (Fig. 3e). The shift of the WPSH to the northeast (the dashed red line in Fig. 3e) leads to the weakness of southeast wind along the boundary of the WPSH. The steering flow at 500 hPa is crucial for TC

Fig. 2 **a** The first mode (EOF1) and **c** the second mode (EOF2) (in units of 10^4 m^2/s^2) leading modes derived from the autumn ACE anomalies in each grid over the WNP for the period 1979–2014 by Japan Meteorological Agency (JMA) best track data (BTD). **b** PC1 and **d** PC2 are the time series of EOF1 and EOF2 derived by using three best track datasets. The black solid line presents PC1 derived from JMA BTD. The red solid line presents PC1 computed from China Meteorological Agency (CMA) BTD. The blue solid line presents PC1 derived from the data of Joint Typhoon Warning Center (JTWC)
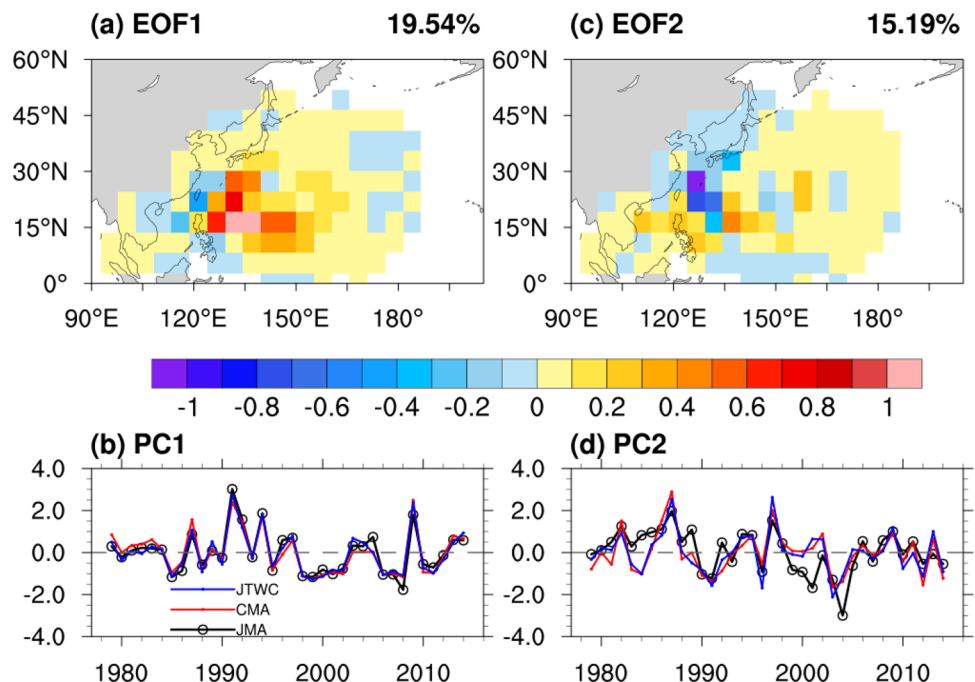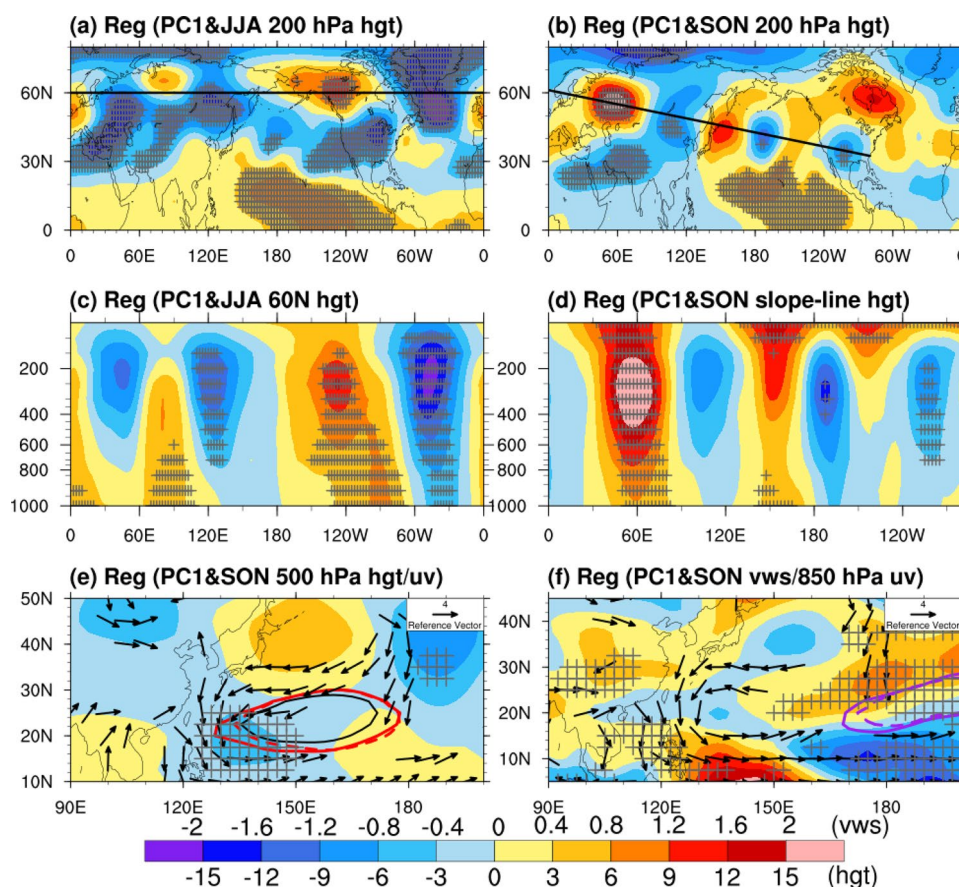
Fig. 3 The regression (color shading) map of PC1 with **a** the June to August (JJA) mean and **b** SON mean 200-hPa geopotential height. The black lines in **a**, **b** mean latitudinal section in **c**, **d**. **c** Section across the latitude of 60°N while **d** across the sloping line crossing the anomalous center. The regression map of PC1 with 500-hPa geopotential height is for **e** the SON mean. The vectors in **e**, **f** represent the 90% significant 500-hPa wind anomalies with PC1 (unit: m/s). The black solid contour in **e** is the long term mean of 5880 geopotential height at 500 hPa (unit: geopotential meter). The red solid

line in **e** is the long term mean 5875 line of geopotential height at 500 hPa. The red dashed line in **e** is the regression of 5875 geopotential height at 500 hPa. The regression map of PC1 is with the vertical wind shear (VWS, sum of the squares of the 200-hPa zonal wind minus the 850-hPa zonal wind, unit: m/s) in **f**. The purple solid line in **f** is the position of the mid-Pacific trough at 200 hPa. The purple dashed line in **f** is the regression position of mid-Pacific trough. The gray cross-shaped markers represent the regression significant at the 90% confidence level

motion. The probability of TC moving to the west of 120° E will decrease under the weakness of the southeast wind. Notably, the mid-Pacific trough moving east in autumn (the dashed purple line in Fig. 3f, identified by relative vorticity of $1 \times 10^{-6}\,\mathrm{s}^{-1}$, Hu et al. 2018) due to the positive anomalous geopotential height in the region from 170° E–150° W and 20° N–40° N (Fig. 3b). Wu et al. (2015) and Wang and Wu (2016) indicated that the shift in the mid-Pacific trough (the purple lines in Fig. 3f) could affect the west–east movement of TC activities.

Meanwhile, some anomalous local conditions occur. Generally, middle-level relative humidity, VWS, relative vorticity, and SST are the most important local conditions for TC genesis and development (Gray 1968). VWS has significant performance in the first mode, with the vector difference of 200 hPa wind and 850 hPa used here. Figure 3f shows

a higher VWS in the region of 120° E–150° E, 5° N–15° N and a smaller VWS along the margin of the WPSH. The stronger VWS hinders the generation and intensification of TCs, causing the decreasing ACE in that region. Under the eastward shift of cyclogenesis, more TC activities cross the region of small VWS, and they are not favored to the west due to the weakness of the southeast steering flow when PC1 is positive. At the same time, the cyclonic anomalies over the Philippine Sea shown at 850 hPa, represent an important system for TC activities (Wang and Chan 2002; Zhou and Cui 2011). TCs wander over the suitable basin and then intensify, this process forms the dipole mode in which one center is the east of the Philippine islands and the other center shows a sloping shape.

To find proper predictors for the dipole mode, we used regression analyses of the time series PC1 on the SST and
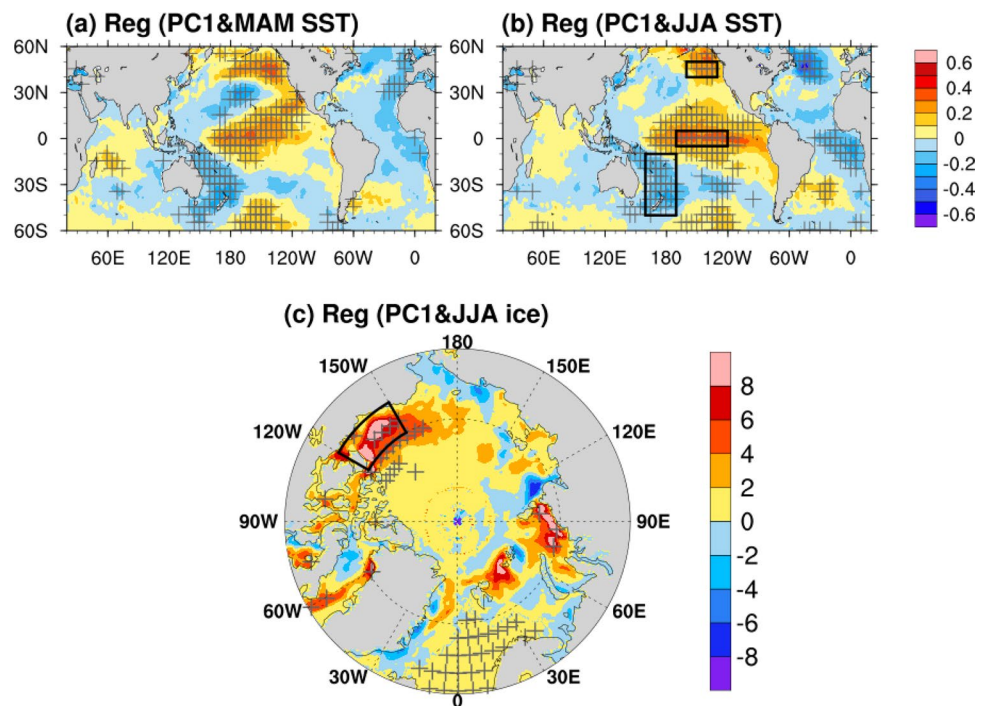
SIC fields. The specific details are illustrated in Fig. 4. The pronounced predictors are shown in SST field: positive SST anomalies continuously appear over the tropical Pacific from MAM (Fig. 4a) to JJA (Fig. 4b); the persistent warming occurs in the Gulf of Alaska; and a large cooling region is present in the southwest Pacific. Meanwhile, the SIC in the Beaufort Sea shows significant positive anomalies in JJA (Fig. 4c). We named these features the four predictors, and their specific areas and meanings shown in Table 1. How do they affect atmospheric circulation over the WNP? We correlated them with the 500-hPa geopotential height/wind and the local VWS, following some results in previous studies, to illustrate two possible pathways.

The anomalous SST in the Gulf of Alaska could induce an anomalous atmospheric wave train (Archambault et al. 2013, 2015, also in Fig. 5c), while the increased sea ice in the Beaufort Sea benefits the barotropic feature of the anomalous wave train (Overland and Wang 2010; Jaiser et al. 2012) and could be a trigger for the anomalous mid-Pacific

trough (Deng et al. 2018) shown in Fig. 5a. At the same time, the anomalous waves train not only influence the position of the WPSH (Fig. 5c), but also cause the shift of the mid-Pacific trough (the black line in Fig. 5b). During the positive PC1 years, the WPSH steering flow on the southwest side of the WPSH weak (Fig. 5a). The eastward of mid-Pacific trough results in the decreased VWS at the east of 145°E (Fig. 5b, d); this situation is consistent with the conclusion in Wu et al. (2015) that it is linked to the weaker westerlies at 200 hPa and the stronger westerlies in the low troposphere that are also physically associated with the variations in the temperature gradient. Both of these features induce the eastern shift of TC activities (Wu et al. 2005, Wang and Wu 2016). Thus, these two predictors have been selected as predictors named the Gulf of Alaska the SST (GASST) and the Beaufort Sea SIC (BFSICE).

Another pathway is the spring Niño 3.4 SST anomalies that cause the deepening of the East Asia trough and the strengthening of the WPSH (Wang and Chan 2002).

Table 1 Definition of each predictor selected for the prediction of the accumulated cyclone energy (ACE) dipole mode

Acronym	Meaning	Definition
BFSICE	The mean of June–July–August Beaufort Sea SIC	MSIC (70° N–75° N, 150° W–120° W)
GASST	The mean of June–July–August Gulf of Alaska SST	MSST (40° N–50° N, 160° W–130° W)
Niño 3.4	The mean of June–July–August Niño 3.4	MSST (5° S–5° N, 170° W–120° W)
SWPSST	The mean of June–July–August Southwest Pacific SST	MSST (50° S–10° S, 160° E–170° W)
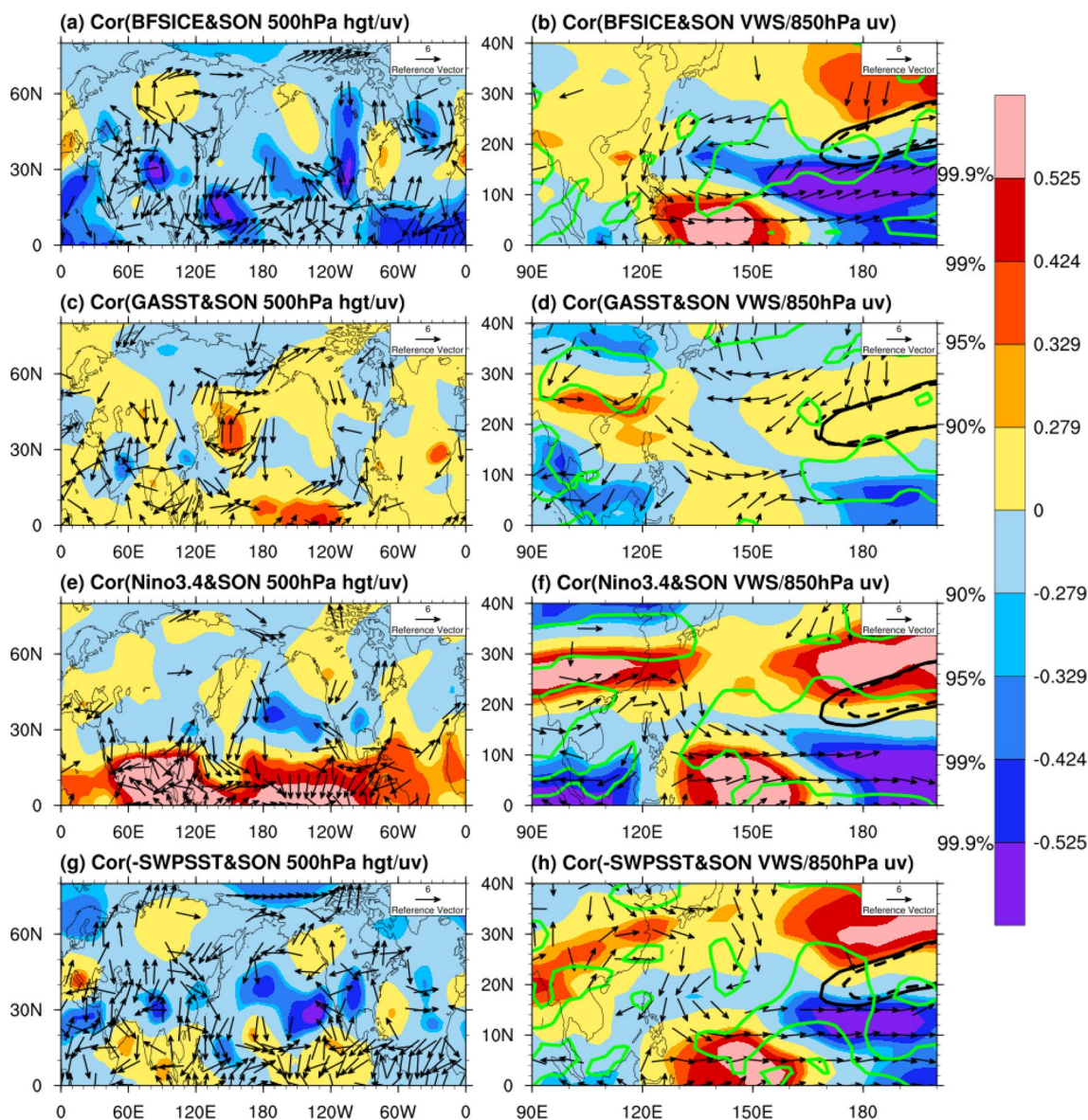
Fig. 5 The correlation map of the SON mean 500-hPa geopotential height (color shading)/the regression map of 500-hPa wind anomalies (vectors) with reference to 0-month lead predictors: **a** JJA mean BFSICE, **c** JJA mean GASST, **e** JJA mean Niño 3.4 and **g** JJA mean SWPSST of PC1. The correlation map of SON local VWS (color shading)/the regression map of 850-hPa anomalous wind (black vec-

tors) with the predictors **b** JJA mean BFSICE, **d** JJA mean GASST, **f** JJA mean Niño 3.4 and **h** JJA mean SWPSST of PC1. The black solid lines in **b**, **d**, **f**, **h** are the long term mean position of the mid-Pacific trough at 200 hPa. The black dashed line in **b**, **d**, **f**, **h** are the regression position of mid-Pacific trough, the green lines show the variation of mid-Pacific trough significant at 95% confidence level, respectively

Similarly, the JJA mean Niño 3.4 SST anomalies are related to a positive anomalous geopotential height over the WNP (Fig. 5e), suppressing the anomalous equator westerly. Wang and Chan (2002) determined that the mechanism can persist in the proceeding fall because the Philippine Sea is dominated by anticyclonic anomalies during El Niño events, which is consistent with Figs. 4 and 5e, f. Matsuura et al. (2003) used a high-resolution coupled general circulation model (CGCM) to prove that the interdecadal TC variability correlated with long-term variations in SST in the tropical

central Pacific. Meanwhile, the negative southwest Pacific SST could affect TC frequency through the anomalous anticyclone over the SCS and the Philippine Sea (Zhou and Cui 2011, also Fig. 5h). The anomalous southwest Pacific SST further shows the influence on the decreased southeast steering flow in Fig. 5g. In fact, the southwest Pacific SST gradient has been used to predict the WNP ACE (Zhan et al. 2013; Zhan and Wang 2016).

Thus, BFSICE and GASST focus on the Northern Hemispheric anomalous wave train, which causes the shift of the

WPSH and mid-Pacific trough and then changes the pattern of the local VWS. Moreover, the Niño 3.4 index and the Southwest Pacific SST (SWPSST) dominate the lower troposphere anticyclonic/cyclonic anomalies to affect ACE. These variables are four predictors on the dipole mode. The detailed definitions of the four predictors for the meridional mode are shown in Table 1.

4.2 The second mode: triple mode

The spatial pattern of the second mode is characterized by three centers including two positive centers, one from the SCS to the Philippine islands, the east of the 135° E line, and a negative center south of the Ryukyu islands that ends at 135° E. Based on the spatial distribution (Fig. 2c), we named the second mode the triple mode. The time series of the triple mode (PC2, Fig. 2d) shows the interannual variability of the triple ACE. The peak values of PC2 are in 1987 and 1997, which differs from PC1 in the dipole mode. In the triple mode, more TCs were active over the SCS and the region east of 135° E and less TC activity occurred between them during the positive PC2 years.

Before searching predictors, we examined the atmospheric anomalies. First, positive 500-hPa geopotential height anomalies appear over South China and east of 150° E (Fig. 6a). There are negative geopotential height anomalies over a large region from the Japanese islands and the Japan Sea across the Korean Peninsula to the northeast of mainland China. This means that the WPSH strengthens on both the west and east sides (the solid red line in Fig. 6a) compared to normal years (The dashed red line in Fig. 6a). Anomalous northwest winds appear north of the WPSH (also in Fig. 6a), hindering the northward TC activities in this region. Second, the local VWS shows a region of significant positive anomalies over the eastern part of the Philippine Sea that inhibits TC genesis and development, as shown in Fig. 6b. According to the wind field anomalies, the anomalous westerlies in both the upper and lower troposphere dramatically contribute to the variation in VWS. Third, the positive 700-hPa relative humidity anomalies over the SCS and South China benefit TC genesis and intensification (Fig. 6c). Finally, corresponding with the negative ACE at the region of 130°–140° E, 20°–35° N, significant negative 850-hPa relative vorticity anomalies hinder TC genesis (Fig. 6d).
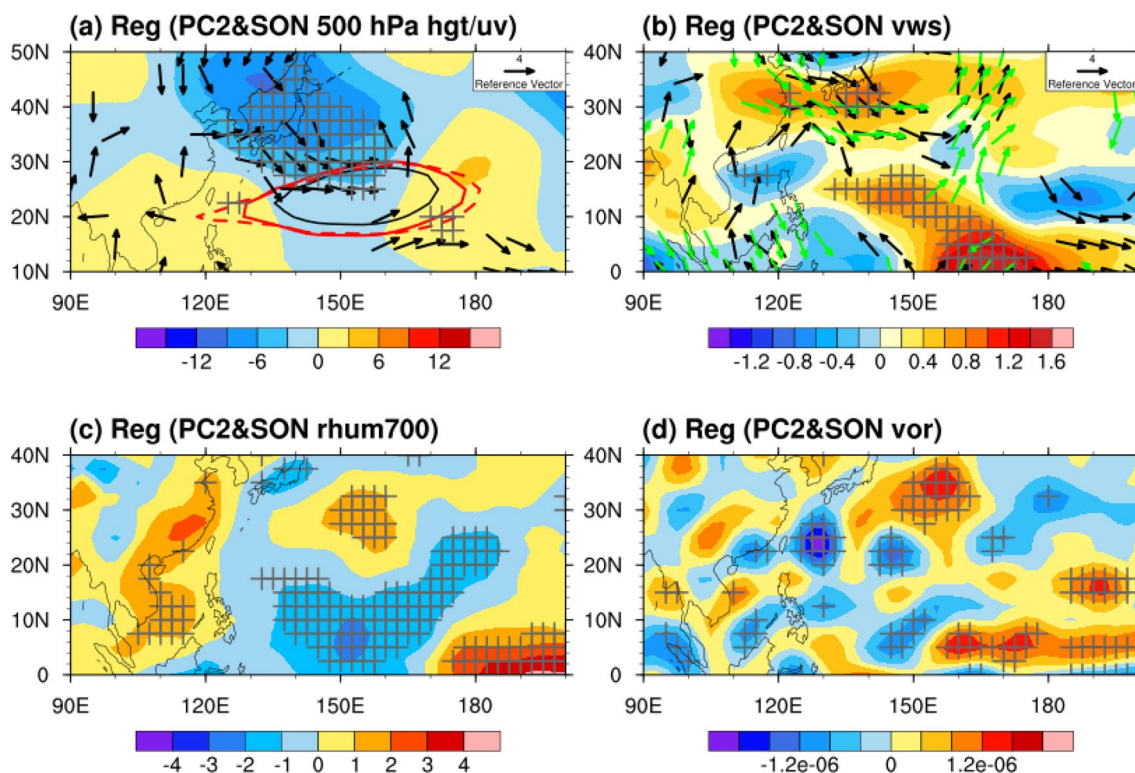
Fig. 6 The regression map of PC2 with 500-hPa geopotential height is for **a** the SON mean. The vectors in **a** represent the 90% significant 500-hPa wind anomalies with PC2 (unit: m/s). The black solid contour in **a** is the long term mean of 5880 geopotential height at 500 hPa (unit: geopotential meter). The red solid line in **a** is the long term mean 5875 line of geopotential height at 500 hPa. The red dashed line in **a** is the regression of 5875 geopotential height at 500 hPa. The regression map of PC2 with **b** VWS, **c** relative humidity at 700 hPa and **d** relative vorticity at 850 hPa. Black vectors in **b** is anomalous wind at 850 hPa and the green vectors is anomalous wind at 200 hPa. The gray cross-shaped markers in **a**–**c** show the regression significant at the 90% confidence level
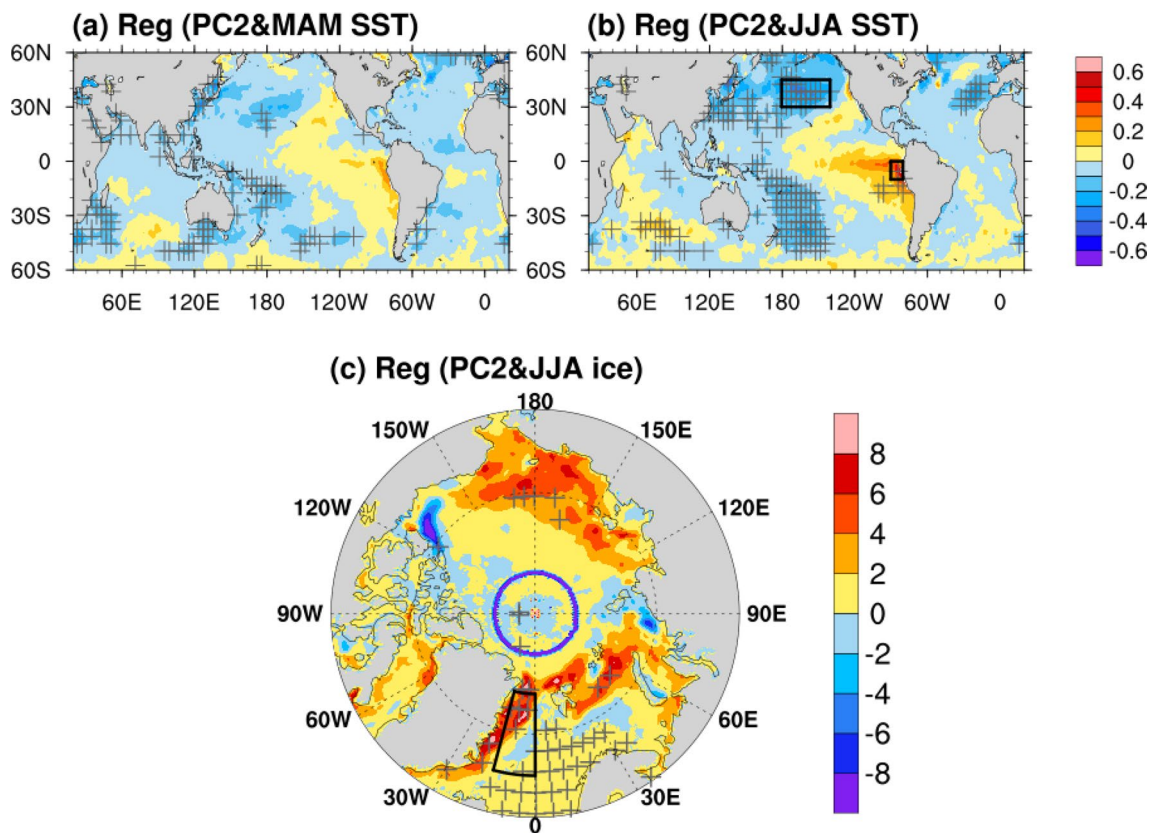
Fig. 7 The same as Fig. 4 but for PC2

To determine the oceanic anomalies that induce changes in the WPSH and local atmospheric conditions, we examined anomalies in SST/SIC during MAM and JJA (Fig. 7). Large regions of the North Pacific and southwest Pacific show cooling signals. Based on the mechanism that the SST of the southwest Pacific can affect WNP TC activities via anticyclonic/cyclonic circulation, no such signal shown in Fig. 6b. Therefore, we excluded the southwest Pacific SST as a predictor. The eastern Pacific is warming but insignificant in spring (Fig. 7a), then the warming proceeding in summer and is much more marked (Fig. 7b). The SIC over the Greenland Sea (GLSICE) is highly associated with the triple ACE mode (Fig. 7c).

The influence of eastern Pacific warming on TC activities has been illustrated in many previous studies. These developing SST warming signals seem to be similar to the eastern Pacific El Niño (Rasmusson and Carpenter 1982). The direct relationship between the difference in the Niño $1+2$ index (Rayner et al. 2003) (JJA mean minus MAM mean) and the local atmosphere is shown in Fig. 8c, d. The large positive correlation of the Niño $1+2$ development index in South China indicates the westward strengthening of the WPSH. The westward reinforced WPSH could enhance the steering flow over the SCS (Fig. 8c) and suppress the convections in

the SCS and the Philippine Sea in both summer and autumn during the eastern Pacific warming events (Wu et al. 2015). At the same time, the eastern Pacific El Niño events indicate the weakening of Walker circulation. Thus, the VWS over the southern part of the SCS and the southeastern WNP is reduced (Fig. 8d). The reduced VWS may enhance the TC activity in the SCS and the eastern part of the WNP. This result is consistent with Fig. 2b.

Arctic sea ice loss could reduce the thermal contrast between tropical and polar regions and then reduce the intensity of the Northern Hemispheric jet streams (Tang et al. 2014; Petrie et al. 2015). The westerlies and VWS over eastern Asia are enhanced during positive GLSICE years (Fig. 8b), this is also consistent with Fig. 6b. Anomalous north wind occurs at 200 hPa on the east side of Taiwan Island during positive GLSICE years, which decrease the TC activity in this region. However, neither the geopotential height nor the wind field at 500 hPa has a significant correlation with GLSICE (Fig. 8a). This result implies that GLSICE affect the atmospheric circulation over eastern Asia and the WNP through upper-level systems, but the details still need more investigation.

The third predictor is the North Pacific SST (NPSST) anomalies, which persistently cool from spring (Fig. 7a)
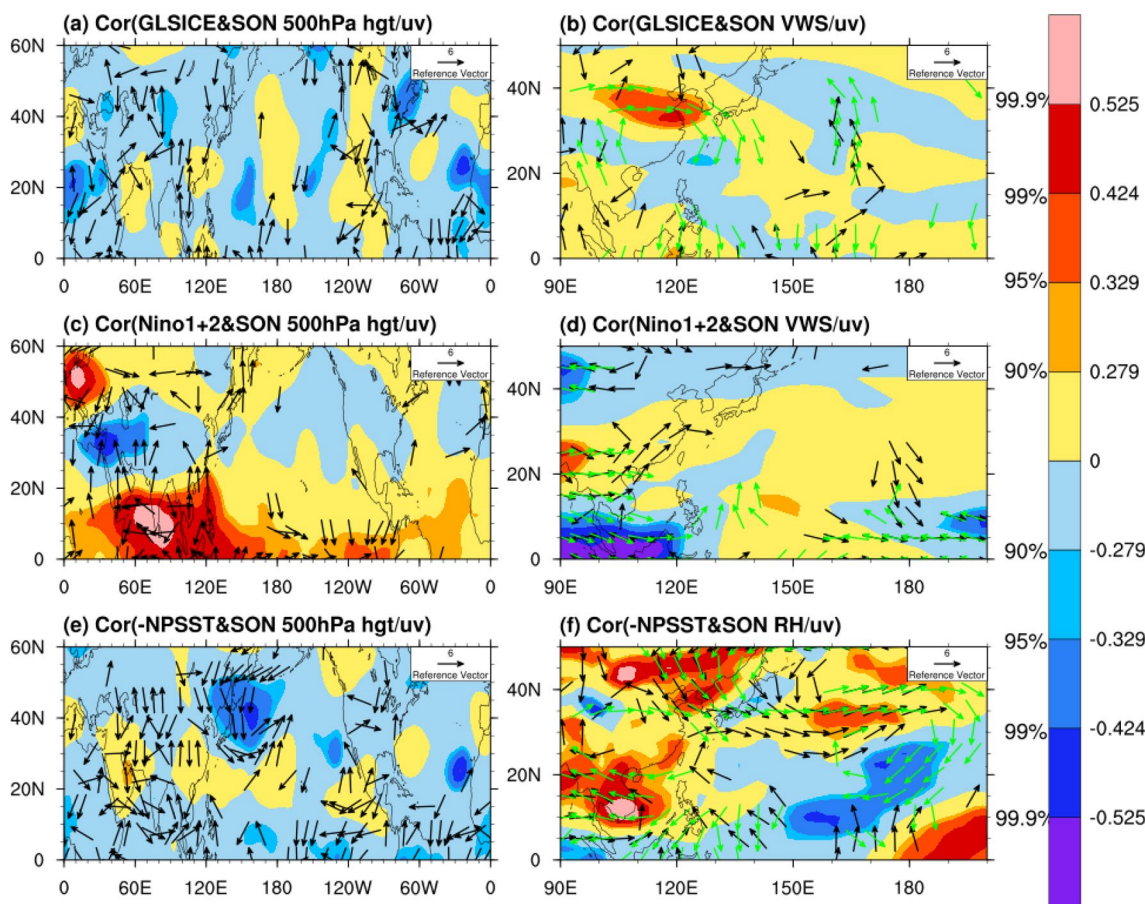
Fig. 8 The correlation map of the SON mean 500-hPa geopotential height (color shading)/wind anomalies (vectors) with reference to 0-month lead predictors: **a** JJA mean GLSICE, **c** JJA mean minus MAM mean Niño 1 + 2 and **e** JJA mean NPSST of PC2. The correlation map of the SON 700-hPa relative humidity (color shading)/850-hPa anomalous wind (black vectors)/200-hPa anomalous wind (green vectors) with the predictors **b** JJA mean GLSICE, **d** JJA mean minus MAM mean Niño 1 + 2 and **f** JJA mean NPSST of PC2

to summer (Fig. 7b) during positive PC2 years. There is a significantly negative anomaly in the 500-hPa geopotential height and associated cyclonic circulations over the region from Korea to the dateline during negative NPSST years (Fig. 8e). The cooling of the NPSST increases the SST gradient from the tropical Pacific to the high latitudes and strengthens the mid-latitude westerlies in both the upper and lower tropospheres (Fig. 8f). In the Philippine Sea, there is an anticyclonic circulation on 850 hPa, which suppress TC activity in this region during negative NPSST years. This

process is an important reason for the negative center of the triple mode.

Overall, these three predictors contribute to either a leading WPSH westward shift or increasing westerlies in the mid-latitudes affecting the local VWS, relative humidity, and relative vorticity. Their definitions are shown in Table 2. Noticeably, the mechanism of how the GLSICE affects the local atmosphere is unclear and requires more research in the future. A relatively clear possible mechanism is based on the second predictor, Niño 1 + 2.

Table 2 Definition of each predictors selected for the prediction of ACE triple mode

Acronym	Meaning	Definition
GLSICE	The mean of June–July–August Greenland Sea SIC	MSIC (70° N–80° N, 15° W–0° W)
NPSST	The mean of June–July–August North Pacific SST	MSST (30° N–45° N, 180°–140° W)
Niño 1 + 2 (JJA-MAM)	The mean of June–July–August minus the mean of March–April–May Niño 1 + 2	DSST (0°–10° S, 90° W–80° W)
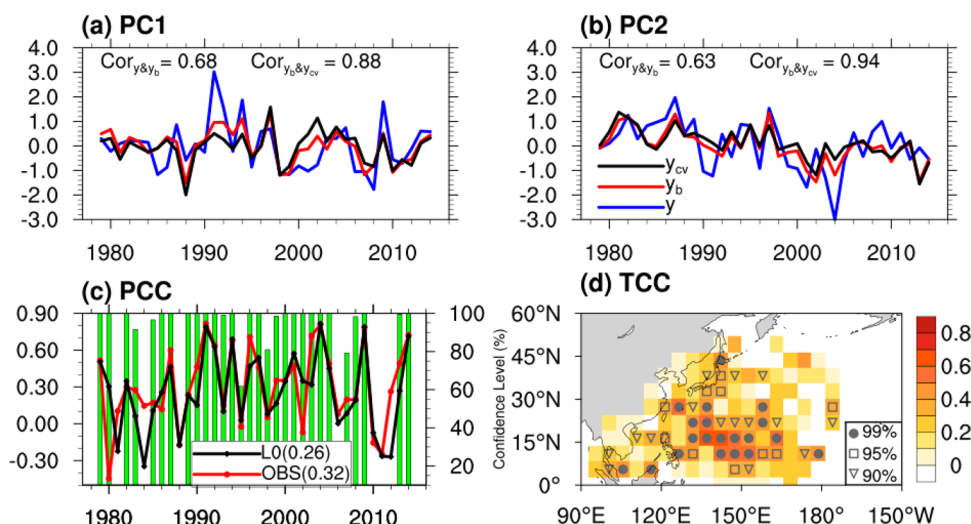
Fig. 9 The corresponding principal component (PCs) are in **a** the first mode and **b** the second mode of observation (OBS) data and cross-validated with physical-empirical predictions by using 0-month lead predictors for 1979–2014. The blue lines are PCs, the red lines are the prediction of PCs and the cross-valid hindcast of PCs are the black lines. **c** Temporal evolution of the pattern correlation coefficient (PCC) skill for the SON ACE distribution over the WNP as a function of the forecast year using 3-year-out cross-validated P–E model predictions (OBS, black lines). The potential attainable forecast skill obtained by using the two observed PCs (L0, red lines). The green bar is the confidence level on prediction. The numbers indicate the long-term mean correlation coefficient for 1979–2014. **d** Temporal correlation coefficient (TCC) skill for the prediction of the SON ACE distribution over the WNP. The gray solid circle markers represent correlation coefficients significant at the 99% confidence level. The gray soft rectangle markers represent correlation coefficients significant at the 95% confidence level. The gray soft triangle markers notify the grid significant at the 90% confidence level

5 Prediction with P–E models and prediction skills

We discuss the two leading EOF modes, which have different predictors and possible pathways. This section discusses prediction skills and real-time prediction of the spatial distribution of ACE. There are two steps for predicting ACE anomalous patterns. First, we predict each PC of the leading modes. Second, the sum of two observed spatial EOF patterns multiplied by their corresponding predicted PCs is used to reconstruct the predicted ACE anomalous field. Third, we compute the predicted ACE pattern by adding the predicted ACE anomalous field to the long-term mean field.

5.1 Prediction with the P–E model

Stepwise multilinear regression is used in the process of establishing the P–E model. Then the cross-validation method makes a retrospective forecast for testing the hindcast experiment skills. The predicted PCs are shown in Fig. 9a, b. The cross-validated correlation skills between the observations and predictions are 0.68 (Fig. 9a) and 0.63 (Fig. 9b) for all 36 years. The correlation coefficients are significant at the 99% confidence level, which means that the two leading modes are regarded as predictable. The predicted PC correlation coefficients with the cross-validated predicted PC are 0.88 and 0.94, reaching the 99% confidence

Table 3 Correlation coefficients between the predictors and the principal component of the first mode (PC1) and among the predictors for the period 1979–2014

	PC1	BFSICE	Niño 3.4	GASST	SWPSST
PC1	**1.0**	**0.41**	**0.38**	**0.42**	**0.52**
BFSICE		**1.0**	0.23	0.21	**− 0.34**
Niño 3.4			**1.0**	0.23	**− 0.53**
GASST				**1.0**	0.18
SWPSST					**1.0**

The bolded numbers (above 0.28 or under − 0.28) represent significance at the 90% confidence level

Table 4 The correlation coefficients between the predictors and the principal component of the second mode (PC2) and among the predictors for the period 1979–2014

	PC2	GLSICE	Niño 1 + 2	NPSST
PC2	**1.0**	**0.38**	**0.29**	**0.44**
GLSICE		**1.0**	0.00	**− 0.32**
Niño 1 + 2			**1.0**	0.24
NPSST				**1.0**

The bolded numbers (above 0.28 or under − 0.28) represent significance at the 90% confidence level

level, which means that the prediction is stable over the long-term period. The prediction equations are as follows:

$$PC1 = 0.191 \times BFSICE + 0.326 \times GASST + 0.260 \times Niño_{3.4} - 0.274 \times SWPSST. \tag{2}$$

$$PC2 = 0.362 \times GLSICE - 0.403 \times NPSST + 0.315 \times Niño_{1+2(JJA-MAM)}. \tag{3}$$

The details of the predictor symbols are presented in Tables 1 and 2.

Some relationships among predictors in PC1 are independent, and the correlation coefficients among predictors are listed in Table 3. The correlation coefficient is 0.21 between BFSICE and GASST, and the correlation coefficient is 0.18 between GASST and SWPSST; they show independent relationships. GASST is also independent of Niño 3.4. Therefore, GASST is an independent factor in the prediction of the dipole mode. Otherwise, the correlation coefficient reaches − 0.53 between Niño 3.4 SST and SWPSST and it reaches − 0.34 between BFSICE and SWPSST. These results imply that SWPSST partly depends on these two predictors. Despite the dependency, a precise physical mechanism associated with the anomaly anticyclone circulation at 850 hPa shows the SWPSST should be a valued predictor of the dipole mode. To explore the necessity of using both SIC and SST indices in predictions, we use two fields to test predictive skills separately. The prediction skill is 0.41 using SIC and 0.60 using SST.

Moving onto PC2, we choose the difference in Niño 1 + 2 between spring and fall as one of the predictors to present the El Niño development events. The correlation coefficient is 0.00 between GLSICE and Niño 1 + 2 (Table 4). The independent relationship between GLSICE and NPSST is − 0.32, which is significant at the 90% confidence level, indicating that the negative correlation between GLSICE and NPSST requires additional studies and that they both influence the mid-latitude anomalous westerlies. In the triple mode, SST in the southwest Pacific is significant, but we excluded this region as a predictor due to the lack of linkage with the lower-level wind field. The significant anomalous SIC in the East Siberian Sea highly depends on the NPSST (the correlation coefficient is − 0.43), and the prediction skill does not improvement, regardless of considering these two regions. The prediction skill is 0.53 when only SST is used to build a predictive equation.

5.2 Prediction skills of ACE distribution

In the previous subsection, we note that the P–E models can potentially predict the two leading EOF modes. The potential pattern correlation coefficient (PCC) is shown in Fig. 9c and is 0.26 for the 36-year mean. The long-term mean PCC skill of prediction is 0.32, which is significant at the 99% confidence level (0.26 for 126 grids). The year-to-year variation is large, with high skill (greater than 0.5) in 1979, 1991, 1992, 1997, 2001, 2004, 2009 and 2014. Years with a low skill (less than 0.0) are 1981, 1984, 1988, 2010, 2011, and 2012. We used lag-one autocorrelation to calculate the degree of effective freedom (Zwiers and Storch 1995; the critical significance level is 0.05 in this study) and tested the confidence level. Twenty-two years significant at the 99% confidence level, and 10 years (the confidence level is less than 90%) predict fails.

Following the PCC skills discussion, the maximum attainable temporal correlation coefficient (TCC) skill is shown in Fig. 9d. Most grids are significant at the 95% or 99% confidence level. Highly predictable regions are found over East Asia, the SCS and the Philippine Sea, consistent with the area where the maximum standard deviation of the location on ACE is located (Fig. 1c). These results show that the P–E model is skillful in the major region influenced by TCs.

To test the predictive validity in real time, we used SST and SIC to calculate the ACE distribution in 2015–2017 using the P–E model. First, we computed the standard deviation of every predictor in 2015–2017. Second, prediction equations were used to obtain the coefficient of the two leading modes. Third, we composited the two leading modes using their variance. Finally, the REEP method was used to remove the grids with a low prediction skill for TC activity. According to the t-test of REEP, the marginal region of TC activities mostly passed the test at the 95% confidence level (figure not shown).The PCC skills are 0.39, 0.70, and 0.41 in 2015, 2016, and 2017, respectively, after applying the REEP method (the valued grids are 79, 66, 69 in 2015–2017, respectively), which are all significant at the 99% confidence level (the degrees of effective freedom are 53, 32, and 21 at 0.05 critical significance level). According to the observation in Fig. 10, the ACE zonal mode played a leading role in 2015 (Fig. 10a), and the recurving track of TCs was dominant in 2016 and 2017 (Fig. 10b, c, respectively). The prediction in 2015 is shown in Fig. 10d. The PCC skill in 2016 was the best. The ACE shapes were similar in 2016 and 2017 (Fig. 10e, f).
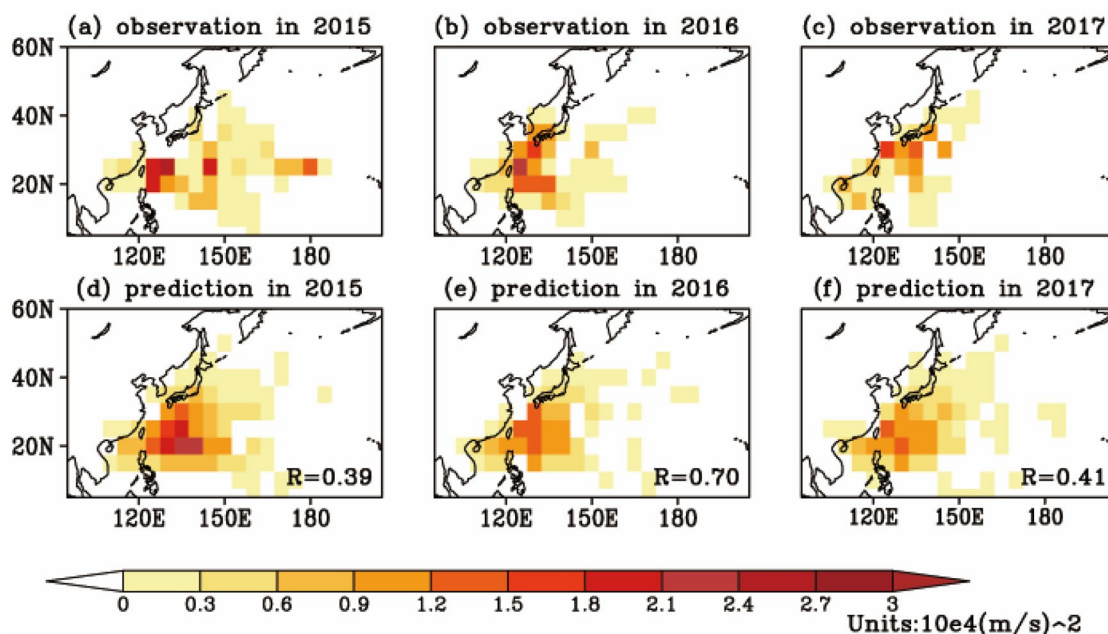
Fig. 10 The **a**–**c** observations and the **d**–**f** corresponding predictions of the ACE distribution over the WNP from SON in **a**, **d** 2015, **b**, **e** 2016, **c**, **f** 2017 (in units of 10^4 m^2/s^2)

6 Conclusions and discussion

We researched the prediction of the ACE over the WNP and found that the distribution of the ACE can be divided into two predictable modes. The first mode represents dipole TC activity; the second mode represents triple TC activity. In the first mode, the anomalous increase in SIC over the Beaufort Sea and the SST warming over the Gulf of Alaska force circumglobal teleconnection anomalous waves in the Northern Hemisphere, causing the WPSH and the mid-Pacific trough to shift to the east. The shift in the WPSH and the mid-Pacific trough induces cyclonic circulation in the lower troposphere and shifts small VWS regions to the east. Moreover, the SST in the southwest Pacific and Niño 3.4 induce anomalous anticyclonic circulation over the SCS and anomaly cyclonic circulation over the Philippine Sea at 850 hPa. Therefore, the TC activity shifts eastward and presents a dipole mode. The second mode is mainly caused by the development of eastern Pacific El Niño events and the cooling of the North Pacific. During the development of El Niño, there are negative VWS anomalies over the southeastern and southwestern WNP and positive VWS anomalies over the central WNP due to the weakened Walker circulation. At the same time, the cooling of NPSST may induce an anticyclonic circulation in the lower troposphere, and the positive anomaly in GLSICE induces anomalous north winds in the upper troposphere over the Philippine Sea. Therefore, TC activity may be enhanced over the SCS and eastern WNP while

it is suppressed over the Philippine Sea during the positive PC2 years, presenting a triple mode.

Then, we used PMA to build a P–E model of TC ACE. To test the prediction skills, mode forecasting skills and time series forecasting skills were used. For the mode forecasting skill, the long-term mean forecasting skill had 99% significance. For the time series forecasting skill, most regions with frequent TC activity passed the 95% significance test, especially in the region near the East Asian mainland and the surrounding islands. On the one hand, the forecasting skill is significant, which shows that the establishment of predictable models is reasonable. On the other hand, the ACE in autumn over the WNP can be divided into dipole and triple modes.

In this study, we focused on the impact of SST and Arctic sea ice anomalies on the distribution of TC ACE over the WNP. These statistically meaningful physical predictors were chosen using only ocean anomalies. The effects of some factors, such as GLSICE in PC2, still need to be revealed. In the future, a pool of predictors, such as atmospheric elements that can improve the ACE prediction skill, needs to be added. In the P–E model, the potentially maximum PCC skill is 0.32, which is almost consistent with the total variance of the interannual variability that accounted for 34.73% of the leading two EOF modes. In other words, the TC activities are more disordered and have a lower potential prediction skill than other weather systems. This P–E model is based on the most recent 36 years (1979–2014). To use this mode persistently, we need to

amend the P–E model by focusing on climate change in the future. Furthermore, this study considers only the 0-month lead P–E hindcast forecast, and we should discuss the few-month lead P–E hindcast forecast in future studies.

References

Archambault HM, Bosart LF, Keyser D et al (2013) A climatological analysis of the extratropical flow response to recurving Western North Pacific tropical cyclones. Mon Weather Rev 141(7):2325–2346. https://doi.org/10.1175/MWR-D-12-00257.1

Archambault HM, Davis CA, Cordeira JM (2015) A composite perspective of the extratropical flow response to recurving Western North Pacific tropical cyclones. Mon Weather Rev 143:1122–1141. https://doi.org/10.1175/MWR-D-14-00270.1

Barcikowska M, Feser F, von Storch H (2012) Usability of best track data in climate statistics in the western North Pacific. Mon Weather Rev 140:2818–2830. https://doi.org/10.1175/MWR-D-11-00175.1

Bell GD, Halpert MS, Ropelewski CF et al (2000) Climate assessment for 1999. Bull Am Meteorol Soc 78(5):s19

Camargo SJ, Emanuel KA, Sobel AH (2007) Use of a genesis potential index to diagnose ENSO effects on tropical cyclone genesis. J Clim 20:4819–4834. https://doi.org/10.1175/JCLI4282.1

Camargo SJ, Wheeler MC, Sobel AH (2009) Diagnosis of the MJO modulation of tropical cyclogenesis using an empirical index. J Atmos Sci 66:3061–3074. https://doi.org/10.1175/2009JAS3101.1

Carr LE, Elsberry RL (1990) Observational evidence for predictions of tropical cyclone propagation relative to environmental steering. J Atmos Sci 47(4):542–546. https://doi.org/10.1175/1520-0469(1990)047<0542:OEFPOT>2.0.CO;2

Chan JCL (1985) Tropical cyclone activity in the Northwest Pacific in relation to the El Niño/Southern Oscillation phenomenon. Mon Weather Rev 113(4):599–606. https://doi.org/10.1175/1520-0493(1985)113<0599:tcaitn>2.0.co;2

Chan JCL (1995) Tropical cyclone activity in the Western North Pacific in Relation to the stratospheric quasi-biennial oscillation. Mon Weather Rev 123(8):2567–2571. https://doi.org/10.1175/1520-0493(1995)123<2567:TCAITW>2.0.CO;2

Chan JCL, Gray WM (1982) Tropical cyclone movement and surrounding flow relationships. Mon Weather Rev 110:1354–1374. https://doi.org/10.1175/1520-0493(1982)110<1354:TCMASF>2.0.CO;2

Choi K, Byun H (2010) Possible relationship between western North Pacific tropical cyclone activity and Arctic Oscillation. Theor Appl Climatol 100:261–274. https://doi.org/10.1007/s00704-009-0187-9

Cohen J, Screen JA, Furtado JC et al (2014) Recent Arctic amplification and extreme mid-latitude weather. Nat Geosci 7(9):627–637. https://doi.org/10.1038/ngeo2234

Demaria M (1985) Tropical cyclone motion in a nondivergent barotropic model. Mon Weather Rev 113(7):1199. https://doi.org/10.1175/1520-0493(1985)113<1199:TCMIAN>2.0.CO;2

Deng K, Yang S, Ting M et al (2018) Variations of the Mid-Pacific trough and their relations to the Asian-Pacific-North American climate: roles of tropical sea surface temperature and Arctic sea ice. J Clim. https://doi.org/10.7916/D8698FZZ

Ding Q, Wang B (2005) Circum-global teleconnection in the northern hemisphere summer. J Clim 18(17):3483–3505. https://doi.org/10.1175/JCLI3473.1

Ding Q, Wang B, Wallace JM, Branstator G (2011) Tropical-extratropical teleconnections in boreal summer: observed inter-annual variability. J Clim 24(7):1878–1896. https://doi.org/10.1175/2011JCLI3621.1

Dong K, Neumann CJ (1986) The relationship between tropical cyclone motion and environmental geostrophic flows. Mon Weather Rev 114:115–122. https://doi.org/10.1175/1520-0493(1986)114<0115:TRBTCM>2.0.CO;2

Du Y, Yang L, Xie S (2011) Tropical Indian Ocean influence on Northwest Pacific tropical cyclones in summer following strong El Niño. J Clim 24:315–322. https://doi.org/10.1175/2010JCLI3890.1

Evans JL, Holland GJ, Elsberry RL (1991) Interactions between a barotropic vortex and an idealized subtropical ridge Part I: vortex motion. J Atmos Sci 48(2):301–314. https://doi.org/10.1175/1520-0469(1991)048<0301:IBABVA>2.0.CO;2

Fan K (2007) North Pacific sea ice cover, a predictor for the Western North Pacific typhoon frequency? Scie China Earth Sci 50(8):1251–1257. https://doi.org/10.1007/s11430-007-0076-y

Gray WM (1968) Global view of the origin of tropical disturbances and storms. Mon Weather Rev 96:669–700. https://doi.org/10.1175/1520-0493(1968)096<0669:GVOTOO>2.0.CO;2

Holland GJ (1983) Tropical cyclone motion: environmental interaction plus a beta effect. J Atmos Sci 40(2):328–342. https://doi.org/10.1175/1520-0469(1983)040<0328:TCMEIP>2.0.CO;2

Holland GJ (1984) Tropical cyclone motion. A comparison of theory and observation. J Atmos Sci 41(1):68–75. https://doi.org/10.1175/1520-0469(1984)041<0068:TCMACO>2.0.CO;2

Hu B, Huang F, Jin P (2015) The relationship between winter extreme minimum temperature events and sea surface temperature and sea ice in China. Clim Change Res Lett 04(3):130–141. https://doi.org/10.12677/ccrl.2015.43015

Hu C, Zhang C, Yang S et al (2018) Perspective on the northwestward shift of autumn tropical cyclogenesis locations over the western North Pacific from shifting ENSO. Clim Dyn 51:2455–2465. https://doi.org/10.1007/s00382-017-4022-1

Jaiser R, Dethloff K, Handorf D et al (2012) Impact of sea ice cover changes on the Northern Hemisphere atmospheric winter circulation. Tellus A Dyn Meteorol Oceanogr 64(1):1–11. https://doi.org/10.3402/tellusa.v64i0.11595

Kim HM, Lee MI, Webster PJ et al (2013) A physical basis for the probabilistic prediction of the accumulated tropical cyclone kinetic energy in the Western North Pacific. J Clim 26(20):7981–7991. https://doi.org/10.1175/JCLI-D-12-00679.1

Klotzbach PJ (2014) Prediction of seasonal Atlantic basin accumulated cyclone energy from 1 July. Weather Forecast 29(1):115–121. https://doi.org/10.1175/WAF-D-13-00073.1

Knapp KR, Kruk MC (2010) Quantifying interagency differences in tropical cyclone best-track wind speed estimates. Mon Weather Rev 138:1459–1473. https://doi.org/10.1175/2009MWR3123.1

Lander M (1994) An Exploratory Analysis of the relationship between tropical storm formation in the Western North Pacific and ENSO. Mon Weather Rev 22:635–651. https://doi.org/10.1175/1520-0493(1994)1222.0.CO;2

Lea A, Saunders MA (2003) Seasonal prediction of total wind energy for tropical storm activity in the Atlantic and North West Pacific. In: EGS-AGU-EUG joint assembly, pp 853–856

Lee C, Camargo SJ, Vitart F, Sobel AH, Tippett MK (2018) Subseasonal tropical cyclone genesis prediction and MJO in the S2S dataset. Weather Forecast 33:967–988. https://doi.org/10.1175/WAF-D-17-0165.1

Lloyd-Hughes B, Saunders MA, Rockett P (2004) A con-solidated CLIPER model for improved August September ENSO prediction skill. Weather Forecast 19:1089–1105. https://doi.org/10.1175/813.1

Luo Z (2001) Effects of tropical cyclone on the short time scale evolution of subtropical high. Acta Meteorol Sin 59(5):549–559. https://doi.org/10.3321/j.issn:0577-6619.2001.05.005

Maloney ED, Hartmann DL (2001) The Madden–Julian oscillation, barotropic dynamics, and North Pacific tropical cyclone formation. Part I: observations. J Atmos Sci 58(17):2545–2558. https://doi.org/10.1175/1520-0469(2001)058<2545:TMJOBD>2.0.CO;2

Matsuura T, Yumoto M, Iizuka S (2003) A mechanism of interdecadal variability of tropical cyclone activity over the western North Pacific. Clim Dyn 21(2):105–117. https://doi.org/10.1007/s00382-003-0327-3

Michaelsen J (1987) Cross-validation in statistical climate forecast models. J Appl Meteor 26(11):1589–1600. https://doi.org/10.1175/1520-0450(1987)026<1589:CVISCF>2.0.CO;2

Miller RG (1964) Regression estimation of event probability. The Trarelens Resear. Cent. Inc, V. S. Wea. Beur., Technical report, 1

Niu L, Huang F, Zhou X (2015) Decadal regime shift of Arctic sea ice and associated decadal variability of Chinese freezing rain. Acta Oceanol Sin 37(11):105–117. https://doi.org/10.3969/j.issn.0253-4193.2015.11.010

North GR, Bell TL, Cahalan RF, Moeng FJ (1982) Sampling errors in the estimation of empirical orthogonal functions. Mon Weather Rev 110(7):699–706. https://doi.org/10.1175/1520-0493(1982)110<0699:seiteo>2.0.co;2

Overland JE, Wang M (2010) Large-scale atmospheric circulation changes are associated with the recent loss of Arctic sea ice. Tellus 62(1):1–9. https://doi.org/10.1111/j.1600-0870.2009.00421.x

Panofsky HA, Brier GW (1968) Some application of statistics to meteorology. Pennsylvania State University Press, University Park

Petrie RE, Shaffrey LC, Sutton RT (2015) Atmospheric response in summer linked to recent Arctic sea ice loss: summertime atmospheric response to Arctic sea ice loss. Q J R Meteorol Soc 141:2070–2076. https://doi.org/10.1002/qj.2502

Rasmusson EM, Carpenter TH (1982) Variations in tropical sea surface temperature and Surface wind fields associated with the Southern Oscillation/El Niño. Mon Weather Rev 110(5):354–384. https://doi.org/10.1175/1520-0493(1982)110<0354:VITSST>2.0.CO;2

Rayner NA, Parker DE, Horton EB et al (2003) Global analyses of sea surface temperature, sea ice, and night marine air temperature since the late nineteenth century. J Geophys Res 108(D14):4407. https://doi.org/10.1029/2002JD002670

Screen JA, Simmonds I (2013) Exploring links between Arctic amplification and mid-latitude weather. Geophys Res Lett 40(5):959–964. https://doi.org/10.1002/grl.50174

Song JJ, Wang Y, Wu L (2010) Trend discrepancies among three best track data sets of western North Pacific tropical cyclones. J Geophys Res 115:D12128. https://doi.org/10.1029/2009JD013058

Tang Q, Zhang X, Francis JA (2014) Extreme summer weather in northern mid-latitudes linked to a vanishing cryosphere. Nat Clim Change 4:45–50. https://doi.org/10.1038/nclimate2065

Wang B, Chan JCL (2002) How strong ENSO events affect tropical cyclone activity over the western North Pacific? J Clim 15:1643–1658. https://doi.org/10.1175/1520-0442(2002)015<1643:HSEEAT>2.0.CO;2

Wang Y, Holland GJ (1996) Tropical cyclone motion and evolution in vertical shear. J Atmos Sci 53:3313–3332. https://doi.org/10.1175/1520-0469(1996)053<3313:tcmaei>2.0.co;2

Wang C, Wu L (2016) Interannual shift of the tropical upper-tropospheric trough and its influence on tropical cyclone formation over the Western North Pacific. J Climate 29:4203–4211. https://doi.org/10.1175/JCLI-D-15-0653.1

Wang B, Zhou X (2008) Climate variation and prediction of rapid intensification in tropical cyclones in the western North Pacific. Meteorol Atmos Phys 99:1–16. https://doi.org/10.1007/s00703-006-0238-z

Wang B, Elsberry RL, Wang Y, Wu L (1998) Dynamics in tropical cyclone motion: a review. Chin J Atmos Sci 22(4):416–434

Wang B, Lee JY, Kang IS, Shukla J (2007) Coupled predictability of seasonal tropical precipitation. Clivar Exchange 12:17–18

Wang B, Xiang B, Lee JY (2013) Subtropical high predictability establishes a promising way for monsoon and tropical storm predictions. Proc Natl Acad Sci 110(8):2718–2722. https://doi.org/10.1073/pnas.1214626110

Wang QY, Li JP, Jin FF et al (2019) Tropical cyclone act to intensify El Niño. Nat Commun 10:3793. https://doi.org/10.1038/s41467-019-11720-w

Wu CC, Emanuel KA (1993) Interaction of a baroclinic vortex with background shear: application to hurricane movement. J Atmos Sci 50(1):62–76. https://doi.org/10.1175/1520-0469(1993)050<0062:ioabvw>2.0.co;2

Wu CC, Kurihara YA (1996) Numerical study of the feedback mechanism of hurricane-environment interaction on hurricane movement from the potential vorticity perspective. J Atmos Sci 53:2264–2282. https://doi.org/10.1175/1520-0469(1996)0532.0.CO;2

Wu L, Wang C, Wang B (2015) Westward shift of western North Pacific tropical cyclogenesis. Geophys Res Lett 42(5):1537–1542. https://doi.org/10.1002/2015GL063450

Xing W, Wang B, Yim SY (2016) Long-lead seasonal prediction of China summer rainfall using an EOF–PLS regression-based methodology. J Clim 29(5):1783–1796. https://doi.org/10.1175/JCLI-D-15-0016.1

Xing W, Wang B, Yim S, Ha K (2017) Predictable patterns of the May–June rainfall anomaly over East Asia. J Geophys Res Atmos 122:2203–2217. https://doi.org/10.1002/2016JD025856

Xu S, Huang F (2010) Super typhoon activity over the western North Pacific and its relationship with ENSO. J Ocean Univ China 9(2):123–128. https://doi.org/10.1007/s11802-010-0123-8

Yim SY, Wang B, Xing W (2014) Prediction of early summer rainfall over South China by a physical–empirical model. Clim Dyn 43(7–8):1883–1891. https://doi.org/10.1007/s00382-013-2014-3

Yim SY, Wang B, Xing W, Lu MM (2015) Prediction of Meiyu rainfall in Taiwan by multi-lead physical–empirical models. Clim Dyn 44(11–12):3033–3042. https://doi.org/10.1007/s00382-014-2340-0

Ying M, Zhang W, Yu H et al (2014) An overview of the China Meteorological Administration tropical cyclone database. J Atmos Ocean Technol 31:287–301. https://doi.org/10.1175/JTECH-D-12-00119.1

Zhan RF, Wang Y (2016) CFSv2-based statistical prediction for seasonal accumulated cyclone energy (ACE) over the Western North Pacific. J Clim 29(2):525–541. https://doi.org/10.1175/JCLI-D-15-0059.1

Zhan RF, Wang Y, Lei XT (2011) Contributions of ENSO and east Indian Ocean SSTA to the inter-annual variability of Northwest Pacific tropical cyclone frequency. J Clim 24:509–521. https://doi.org/10.1175/2010JCLI3808.1

Zhan R, Wang Y, Wen M (2013) The SST gradient between the Southwestern Pacific and the Western Pacific warm pool: a new factor controlling the Northwestern Pacific tropical cyclone genesis frequency. J Clim 26(7):2408–2415. https://doi.org/10.1175/JCLI-D-12-00798.1

Zhou B, Cui X (2011) Sea surface temperature east of Australia: a predictor of tropical cyclone frequency over the western North Pacific? Chin Sci Bull 56(2):196–201. https://doi.org/10.1007/s11434-010-4157-5

Zhou X, Huang F (2015) Decadal shift of the extreme high temperature in China and its relationship with sea surface temperature. J Ocean Univ China 45(5):19–27. https://doi.org/10.16441/j.cnki.hdxb.20140057

Zwiers FW, Storch HV (1995) Taking serial correlation into account in tests of the mean. J Clim 8:336–351. https://doi.org/10.1175/1520-0442(1995)008<0336:TSCIAI>2.0.CO;2